Quantum anomalous Hall phase in (001) double-perovskite monolayers via intersite spin-orbit coupling

Hongbin Zhang,[1,*] Huaqing Huang,[1,2] Kristjan Haule,[1] and David Vanderbilt[1]
[1]*Department of Physics and Astronomy, Rutgers University, Piscataway, New Jersey 08854, USA*
[2]*Department of Physics, Tsinghua University, Beijing 100084, China*
(Received 13 June 2014; revised manuscript received 7 October 2014; published 30 October 2014)

Using tight-binding models and first-principles calculations, we demonstrate the possibility to achieve a quantum anomalous Hall (QAH) phase on a two-dimensional square lattice, which can be realized in monolayers of double perovskites. We show that effective intersite spin-orbit coupling between e_g orbitals can be induced perturbatively, giving rise to a QAH state. Moreover, the effective spin-orbit coupling can be enhanced by octahedral rotations. Based on first-principles calculations, we propose that this type of QAH state could be realized in La_2MnIrO_6 monolayers, with the size of the gap as large as 26 meV in the ideal case. We observe that the electronic structure is sensitive to structural distortions, and that an enhanced Hubbard U tends to stabilize the nontrivial gap.

DOI: 10.1103/PhysRevB.90.165143 PACS number(s): 72.80.Vp, 75.47.−m, 81.05.ue

I. INTRODUCTION

The quantum anomalous Hall (QAH) effect has drawn intensive attention recently, in part due to the dissipationless transport that can take place in the spin-polarized edge states, which are topologically protected against perturbative disorder. A generic model to achieve the QAH phase was first proposed by Haldane on the honeycomb lattice [1], where complex hoppings between next-nearest neighbors (NNNs) play a crucial role. Several systems have been proposed to host such nontrivial topological phases, such as magnetically doped topological insulators [2,3] and honeycomb lattices formed by transition-metal or heavy-metal ions [4–8]. For most of these systems, the occurrence of the QAH phase relies on the honeycomb lattice, and the topological properties are usually carried by the sp bands. Meanwhile, spontaneous time-reversal symmetry breaking is usually induced by doping with magnetic ions or via a magnetic proximity effect. These two limitations greatly reduce the range of available candidate systems to search for the occurrence of a QAH state. In Cr-doped $(Bi_{1-x}Sb_x)_2Te_3$, for example, where the QAH phase has first been observed experimentally [9], the QAH effect is only observable below about 30 mK, due to the small exchange splittings induced by Cr doping.

In their seminal work, Xiao *et al.* proposed that in (111) superlattices of perovskite transition-metal oxides (TMOs), various topological phases can be obtained [10]. For TMOs with partially occupied d shells, magnetism is relatively easy to obtain because the d electrons are more localized than the sp electrons. Furthermore, electronic correlations are usually significant in TMOs with localized d electrons, and there is the possibility that nontrivial topological phases can develop by spontaneous symmetry breaking [11–13] with a dynamically generated spin-orbit coupling (SOC) [14]. It has even been theoretically argued that nontrivial topological phases can be realized in (111) TMO heterostructures without considering atomic SOC [15–17]. In all these proposals, the underlying honeycomb lattice facilitates the appearance of a topological phase. Unfortunately, it is difficult to synthesize (111) TMO superlattices experimentally with good atomic precision, although there has been some recent experimental progress in this direction [18].

The presence of a honeycomb lattice is not, however, a necessary condition for the occurrence of the QAH effect. For instance, topologically nontrivial phases can be obtained on square lattices with well-designed nearest-neighbor (NN) and NNN hoppings [19–22]. Recently, three proposals have been put forward to achieve the QAH effect in more realistic systems based on square-lattice symmetry, i.e., superlattices of CdO/EuO [23] and GdN/EuO [24] with the rocksalt structure and CrO_2/TiO_2 with the rutile structure [25]. For the latter case, the relevant bands are the t_{2g} states of Cr; while these states show large exchange splittings, the topological gap is only about 4 meV due to the small strength of the onsite atomic SOC of Cr atoms.

In this work, we demonstrate the possibility of achieving a nontrivial QAH phase in (001)-oriented double-perovskite monolayers. Using a two-band model for e_g orbitals on a square lattice, we show that complex effective intersite hoppings between two e_g orbitals can be induced perturbatively by the atomic SOC, giving rise to a QAH state. Based on first-principles calculations, we further show that such a model can be realized in checkerboard La_2MnIrO_6 (LMIO) monolayers (ML) embedded in a nonmagnetic insulating host such as $LaAlO_3$ (LAO). The magnitude of the topological gap in the ideal case can be as large as 26 meV. The advantage of such a system is that (001) superlattices of perovskite compounds are well studied and can be synthesized with good atomic precision, resulting in controlled structural properties. Moreover, given the abundance of physical properties in perovskite TMO superlattices, including high-T_c superconductivity [26], the QAH phase realized in (001) perovskite superlattices can also be integrated more easily with other functional oxides to achieve new physical properties.

*Corresponding author: hzhang@physics.rutgers.edu

The paper is organized as follows. In Sec. II, we present the tight-binding model for half-filled e_g states on a square lattice. We demonstrate how the effective SOC can be induced following standard perturbation theory, focusing on the role of octahedral rotations. Detailed symmetry analysis is given to understand how the nontrivial topological phase develops. Our first-principles results are shown in Sec. III, where the model arguments in Sec. II are verified by considering a hypothetical structure. The effects of structural relaxations are then studied in detail and it is shown that epitaxial strain can be used to tune the LMIO monolayers close to the critical region where a nontrivial QAH state exists.

II. TWO-BAND MODEL

Our tight-binding model simulates a double-perovskite ML with checkerboard ordering of the two sublattices, either isolated in vacuum or embedded in an inert (wide-gap nonmagnetic) perovskite host. To be specific, we consider a case in which one sublattice is populated with ions having large exchange splittings, typically high-spin $3d$ transition-metal ions, while ions with filled (e.g., t_{2g}) subshells, preferably with large onsite SOC, are located on the other sublattice. In this work, we consider the combination of Mn^{3+} and Ir^{3+} ions as an example, as it will turn out to be a promising candidate based on our first-principles calculations in Sec. III.

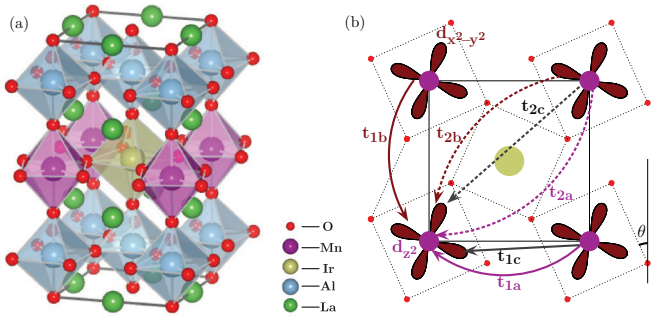

FIG. 1. (Color online) (a) Oblique view of the crystal structure of an La_2MnIrO_6 (LMIO) monolayer (ML) sandwiched between $LaAlO_3$ layers. (b) Sketch defining the parameters of the tight-binding model of Eq. (1) that describes the LMIO ML. Only the local e_g orbitals on Mn atoms (purple, at origin) are shown; orbitals on Ir (brown, at the center) are suppressed. The intersite hoppings between Mn e_g orbitals on nearest neighbors (t_{1i}) and next-nearest neighbors (t_{2i}) are shown by arrows (see main text for details). The octahedral rotations, denoted by angle θ in (b), are exaggerated for clarity of illustration.

The crystal structure of such an LMIO monolayer sandwiched between LAO layers is shown in Fig. 1(a). The corresponding tight-binding model for the two e_g orbitals on each Mn site can be expressed in the local $(d_{z^2}, d_{x^2-y^2})$ basis as

$$H = \begin{pmatrix} t_{1a}\, f_1(\mathbf{k}) + t_{2a}\, f_2(\mathbf{k}) & (t_{1c} - i\lambda^{(1)})\, g_1(\mathbf{k}) - (t_{2c} - i\lambda^{(2)})\, g_2(\mathbf{k}) \\ \text{c.c.} & \Delta + t_{1b}\, f_1(\mathbf{k}) + t_{2b}\, f_2(\mathbf{k}) \end{pmatrix}, \tag{1}$$

where $f_1(\mathbf{k}) = \cos k_x + \cos k_y$, $g_1(\mathbf{k}) = \cos k_x - \cos k_y$, $f_2(\mathbf{k}) = 2\cos k_x \cos k_y$, and $g_2(\mathbf{k}) = 2\sin k_x \sin k_y$. The model is parametrized by the difference Δ between the onsite energies of $d_{x^2-y^2}$ and d_{z^2} orbitals, the NN hoppings t_{1i}, the NNN hoppings t_{2i}, and the effective SOC parameters $\lambda^{(1)}$ and $\lambda^{(2)}$, which respectively denote the NN and NNN couplings between d_{z^2} and $d_{x^2-y^2}$ orbitals induced perturbatively as explained in the following. For the hoppings t_{1i} and t_{2i}, $i = a$ or b refers to the like-orbital hopping between d_{z^2} or $d_{x^2-y^2}$ orbitals, respectively, while $i = c$ denotes the unlike-orbital hopping between d_{z^2} and $d_{x^2-y^2}$ orbitals. Note that these are all "effective hoppings" in the sense that the oxygen and iridium orbitals are regarded as having been integrated out.

The complex hopping terms $i\lambda^{(1)}$ and $i\lambda^{(2)}$ in Eq. (1) between d_{z^2} and $d_{x^2-y^2}$ orbitals can be induced by considering perturbative processes involving SOC. When there is no rotation of the transition-metal-oxygen octahedra, the $i\lambda^{(1)}$ term arises following

$$i\lambda^{(1)} = \frac{\langle d_{z^2}^{\mathrm{Mn}} | \hat{H} | d_{xy}^{\mathrm{Mn}} \rangle \langle d_{xy}^{\mathrm{Mn}} | \xi^{\mathrm{Mn}} \hat{\mathbf{L}} \cdot \hat{\mathbf{S}} | d_{x^2-y^2}^{\mathrm{Mn}} \rangle}{E_{e_g}^{\mathrm{Mn}} - E_{t_{2g}}^{\mathrm{Mn}}}, \tag{2}$$

where $\hat{\mathbf{L}}$ ($\hat{\mathbf{S}}$) is the orbital (spin) angular-momentum operator, ξ^{Mn} is the strength of the atomic SOC on Mn, and $\hat{H}$ denotes direct hybridization between d_{xy} and d_{z^2} orbitals located on NN Mn sites. $E_{t_{2g}}^{\mathrm{Mn}}$ and $E_{e_g}^{\mathrm{Mn}}$ denote the onsite energies of the t_{2g} and e_g subshells on the Mn ions in the cubic crystal field. In a general case when the in-plane rotation angle θ [cf. Fig. 1(b)] is nonzero, it can be shown that $i\lambda^{(1)} \propto i\xi^{\mathrm{Mn}} \sin(2\theta^{\mathrm{Mn}}) = i\xi^{\mathrm{Mn}} \cos(2\theta)$, where θ^{Mn} denotes the rotation angle of the MnO_6 octahedra and $\theta^{\mathrm{Mn}} = \theta + 45^\circ$. That is, $i\lambda^{(1)}$ is an even function of the rotation angle θ. We note that second-order processes involving Ir t_{2g} orbitals can also lead to an effective SOC between the e_g orbitals located on NN Mn sites, but the two most obvious contributions, corresponding to hopping via the two Ir atoms adjacent to a given Mn-Mn bond, tend to cancel one another.

A finite rotation angle θ leads to a nonzero $i\lambda^{(2)}$ term between e_g orbitals located on NNN Mn sites. It arises following

$$i\lambda^{(2)} = \frac{\langle d_{z^2}^{\mathrm{Mn}} | \hat{H}' | d_{xy}^{\mathrm{Ir}} \rangle \langle d_{xy}^{\mathrm{Ir}} | \xi^{\mathrm{Ir}} \hat{\mathbf{L}} \cdot \hat{\mathbf{S}} | d_{x^2-y^2}^{\mathrm{Ir}} \rangle \langle d_{x^2-y^2}^{\mathrm{Ir}} | \hat{H}' | d_{x^2-y^2}^{\mathrm{Mn}} \rangle}{(E_{e_g}^{\mathrm{Ir}} - E_{t_{2g}}^{\mathrm{Ir}})(E_{e_g}^{\mathrm{Mn}} - E_{e_g}^{\mathrm{Ir}})}, \tag{3}$$

where ξ^{Ir} denotes the strength of the atomic SOC on Ir sites, $E_{t_{2g}}^{\mathrm{Ir}}$ and $E_{e_g}^{\mathrm{Ir}}$ are the onsite energies of the Ir t_{2g} and e_g orbitals, and $\hat{H}'$ denotes the direct hybridization between orbitals on Mn and Ir atoms. Similar virtual transitions involving coupling of the $d_{x^2-y^2}^{\mathrm{Mn}}$ orbital of Mn to the d_{xy}^{Ir} orbital of Ir also lead to nonzero contributions. The resulting total $i\lambda^{(2)} \propto i\xi^{\mathrm{Ir}} \sin(2\theta)$, with θ the octahedral rotation angle. That is, $i\lambda^{(2)}$ is an odd function of θ. Furthermore, the magnitude of $\lambda^{(2)}$ is determined

by the strength of the atomic SOC of the Ir atoms. We observe that for the LMIO monolayers considered in this work, the magnitude of $\lambda^{(2)}$ is about one order of magnitude larger than that of $\lambda^{(1)}$, due to the much stronger atomic SOC of Ir ($\sim$0.5 eV) compared to that of Mn ($\sim$0.05 eV).

The Hamiltonian in Eq. (1) is fully consistent with the symmetry requirements. Our analysis reveals that there are four kinds of symmetry operations that are important: twofold rotations C_2 centered at the midpoints of NN Mn-Mn bonds, twofold rotations C_2 centered at the Ir sites, mirrors $M'_{x/y}$ with respect to a plane connecting the centers of the NN Mn-Mn bonds along either x or y, and mirrors M'_d connecting NNN Mn sites. Here, the rotational axes and mirror planes are all perpendicular to the MnIr plane, and M' denotes a combination of a mirror and the time-reversal operations. A detailed analysis (cf. Appendix) confirms that both $\lambda^{(1)}$ and t_{2c} are even functions of the rotational angle θ, and both $\lambda^{(2)}$ and t_{1c} are odd functions of θ, leading to the Hamiltonian shown in Eq. (1).

The two-band model of Eq. (1) can be solved analytically by decomposing the Hamiltonian as $H = \sigma_0 h_0 + \sum_{i=1}^{3} h_i \sigma_i$ where σ_0 is the unit matrix and σ_i are the Pauli matrices. The Berry curvature for the lower-lying band can be obtained explicitly as

$$\Omega = -\frac{2}{h}\frac{\epsilon_{ijk}\, h_i h_{jx} h_{ky}}{(E_+ - E_-)^2}, \tag{4}$$

where ϵ_{ijk} is the Levi-Civita symbol, $h = \sqrt{h_1^2 + h_2^2 + h_3^2}$, $h_{i\alpha} = \partial h_i / \partial k_\alpha$ ($\alpha = x, y$), and $E_\pm = h_0 \pm h$ are the energy eigenvalues for the higher/lower bands. In our case,

$$\begin{aligned} h_0 &= [\Delta + (t_{1a} + t_{1b}) f_1(\mathbf{k}) + (t_{2a} + t_{2b}) f_2(\mathbf{k})]/2, \\ h_1 &= t_{1c} g_1(\mathbf{k}) - t_{2c} g_2(\mathbf{k}), \\ h_2 &= \lambda^{(1)} g_1(\mathbf{k}) - \lambda^{(2)} g_2(\mathbf{k}), \\ h_3 &= [-\Delta + (t_{1a} - t_{1b}) f_1(\mathbf{k}) + (t_{2a} - t_{2b}) f_2(\mathbf{k})]/2. \end{aligned} \tag{5}$$

The band structure obtained from a model of this form is presented in Fig. 2(a), and the regions of strong Berry curvature, corresponding to small direct gaps, are shown as the (blue/red) shaded regions in Figs. 2(b)–2(d). The diagonal hopping parameters for the plots were obtained by fitting to the first-principles band structure of Fig. 3(b), yielding $t_{1a} = -0.27$ eV, $t_{1b} = 0.09$ eV, $t_{2a} = 0.05$ eV, $t_{2b} = -0.105$ eV, and $\Delta = 0.28$ eV. The off-diagonal terms were set to $t_{1c} = 0.02$ eV, $t_{2c} = 0.02$ eV, $\lambda^{(1)} = 0.02$ eV, and $\lambda^{(2)} = 0.08$ eV. The inset of Fig. 2(a) shows the computed edge states for an 80-unit-cell-wide ribbon cut from this model, providing the first evidence that the model exhibits a nontrivial topology.

To understand how these features of the band structure come about, it is useful to return to Eqs. (4) and (5). Note that h_1 and h_2 both have to be present in order to obtain a nonzero Berry curvature. Actually, we find that nonzero t_{2c} and $\lambda^{(1)}$ or nonzero t_{1c} and $\lambda^{(2)}$ can both lead to nontrivial topological phases, corresponding to the case without rotations and the case with only terms induced by rotations, respectively. Interestingly, the Chern numbers are of opposite sign for the two cases. Due to the much larger magnitude of $\lambda^{(2)}$, the Chern number of the system is determined in practice by the combination of t_{1c} and $\lambda^{(2)}$.

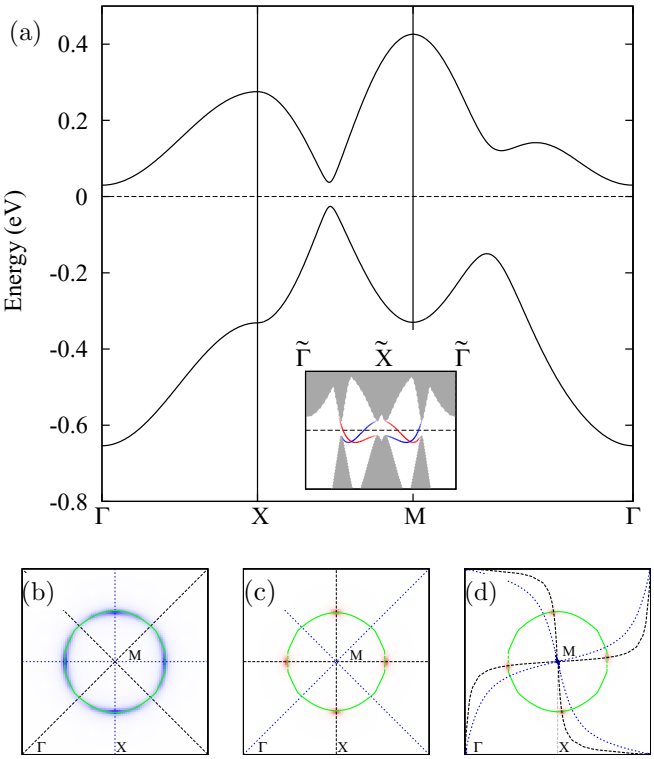

FIG. 2. (Color online) Electronic structure of the tight-binding model of Eq. (1) with parameters as given in the text. (a) Band structure along the high-symmetry Γ-X-M-Γ k path. Inset shows the projected bulk band structure (shaded region) and edge states for an 80-unit-cell-wide ribbon in the reduced 1D BZ along $\tilde{\Gamma}$-$\tilde{X}$-$\tilde{\Gamma}$, color coded to distinguish the contributions from the two edges; dashed line denotes E_F. (b)–(d) Color map showing the distribution of negative (blue) and positive (red) Berry curvature in the BZ for three cases: (b) without octahedral rotations (t_{2c} and $\lambda^{(1)}$ nonzero); (c) with octahedral rotations (t_{1c} and $\lambda^{(2)}$ nonzero) but t_{2c} and $\lambda^{(1)}$ artificially set to zero; and (d) with octahedral rotations, including all four terms. For guidance, nodes of h_1, h_2, and $h_0 + h_3$ in Eq. (5) are shown as dotted blue, dashed black, and solid green curves, respectively.

Consider first the case that the octahedral rotation angle θ vanishes. Then, $t_{1c} = 0$ because symmetry prevents any direct hybridization of d_{z^2} and $d_{x^2-y^2}$ orbitals on NN Mn sites. In this case, $\lambda^{(2)} = 0$ as well because the hybridization of d_{z^2} and $d_{x^2-y^2}$ orbitals on NNN Mn sites via Ir atoms is forbidden. In fact, we observed that both t_{1c} and $\lambda^{(2)}$ are proportional to $\sin 2\theta$, as explained above for $\lambda^{(2)}$. That is, without octahedral rotations only t_{2c} and $\lambda^{(1)}$ in the off-diagonal terms of Eq. (1) are nonzero. Examining Eq. (1) reveals that without the off-diagonal terms proportional to $\lambda^{(1)}$ and t_{2c}, the eigenvalues of the Hamiltonian are degenerate wherever $h_3 = 0$, which turns out to be a loop centered at the M point in the Brillouin zone (BZ) as shown by the green lines in Fig. 2(b). This reflects the fact that neither $f_1(\mathbf{k})$ nor $f_2(\mathbf{k})$ vanishes in the vicinity of M. By contrast, $g_1(\mathbf{k})$ vanishes along the Γ-M lines, while $g_2(\mathbf{k})$ vanishes along the X-M lines, as indicated by the (black) dashed and (blue) dotted lines in Fig. 2(b), respectively. Thus, the loop of degeneracy is reduced to four points (Dirac nodes)

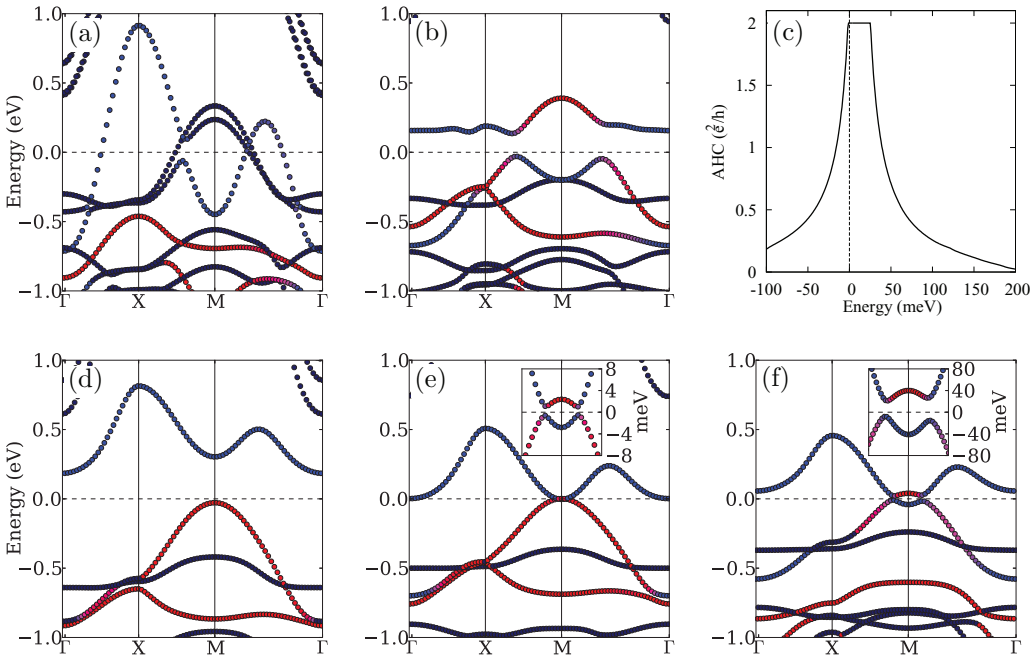

FIG. 3. (Color online) Electronic structures of the LMIO/LAO superlattices. Red (blue) color coding highlights the character of the d_{z^2} ($d_{x^2-y^2}$) orbitals of the Mn atoms, and black indicates the Ir-5d states. All calculations are done with $U = 5.0$ eV and $J = 1.0$ eV on Mn unless stated otherwise. (a) Hypothetical structure without octahedral rotations (see main text for details). (b) Hypothetical structure with 15° rotations about the z axis in the LMIO layers only. (c) Calculated anomalous Hall conductivity for case (b). (d) Relaxed structure at zero epitaxial strain. (e) Relaxed structures at 2% tensile epitaxial strain. (f) Same as (e) but with U on Mn sites increased to 7.0 eV. Insets in (e) and (f) zoom in on the region around the M point. Dashed lines denote the Fermi energies.

located on the X-M directions if $\lambda^{(1)}$ is turned on, or on the Γ-M lines if t_{2c} is turned on.

When both $\lambda^{(1)}$ and t_{2c} are nonzero, the energy spectrum of Eq. (1) is fully gapped, leaving concentrations of Berry curvature in the regions of the BZ where the gap is small, as shown by the (blue) shading in Fig. 2(b). Since the magnitude of $\lambda^{(1)}$ is comparable to that of t_{2c}, the distribution of the Berry curvature is quite smeared. The resulting total Chern number is $C = -2$ after integrating the Berry curvature over the whole BZ, indicating that a QAH state has been formed. This is confirmed by our numerical calculation of the anomalous Hall conductivity (AHC), which we find to be equal to $-2\,e^2/h$.

Switching on the octahedral rotations modifies the hybridization between d orbitals of Mn and Ir atoms, renormalizing all the hopping parameters in Eq. (1). However, we find that the most important changes arise from the fact that t_{1c} and $\lambda^{(2)}$ adopt nonzero values when $\theta \neq 0$. To characterize the influence of these two terms, we first consider an artificial situation in which t_{1c} and $\lambda^{(2)}$ are turned on while t_{2c} and $\lambda^{(1)}$ are turned off, with all other parameters kept fixed at their previous values. As shown in Fig. 2(c), the sharpest concentrations of Berry curvature are found in monopolelike peaks; these lie on the X-M lines because $|t_{1c}| < |\lambda^{(2)}|$. The Chern number that results by integrating the Berry curvatures over the BZ is now $C = 2$, opposite to the case when t_{2c} and $\lambda^{(1)}$ are nonzero. This sign reversal results from the fact that the $\lambda^{(1)}$ and $\lambda^{(2)}$ terms are of opposite sign [cf. Eq. (1)].

Figure 2(d) shows the distribution of the Berry curvature and the corresponding nodes of the h_1, h_2, and $h_0 + h_3$ defined in Eq. (5) when the full Hamiltonian of Eq. (1) is considered, including both the preexisting interactions and those induced by rotations. Since $\lambda^{(1)}$ and $\lambda^{(2)}$ have different k dependencies as given in Eq. (1), the nodes of h_2 shift slightly in the counterclockwise direction relative to the case of Fig. 2(c). There is also a shift (larger and in the opposite direction) in the nodes of h_1 arising from the competition between t_{1c} and t_{2c}. However, because of the large magnitude of $\lambda^{(2)}$, the avoided crossings follow the nodes of h_2. The result is that the four avoided-crossing points of the full Hamiltonian are rotated slightly in the counterclockwise direction around M compared to Fig. 2(c). Moreover, the topological properties of our model are dominated by the combination of $\lambda^{(2)}$ and t_{1c}, so that the Chern number is $C = 2$. That is, the octahedral rotations induce a topological phase transition where the Chern number changes from -2 to 2. The topological nontriviality is also confirmed by an explicit calculation of the edge states of a one-dimensional (1D) ribbon as shown in the inset of Fig. 2(a). It is evident that two edge states with the same group velocity are located on one edge, while another two edge states with the opposite group velocity are located on the other edge.

The fact that the absolute value of the Chern number is two, and not one, can be understood in several ways. For example, we note that in the limit of a very small coefficient of g_2, so that the four Dirac points are just barely opened, each should carry a Berry phase of $\pm\pi$ (as is standard for a simple avoided Dirac crossing); four of them add to $\pm 4\pi$, suggesting $C = \pm 2$. Another approach is to consider the limit that the four degeneracy points shrink to the M point and merge. Specifically, we find that by tuning Δ, the difference between onsite energies of valence d_{z^2} and conduction $d_{x^2-y^2}$

orbitals in the tight-binding model, the four avoided crossings shrink to a singular point with *quadratic* dispersion at M when $\Delta_c = 1.034$ eV, and the gap reopens in a normal $C = 0$ phase for $\Delta > \Delta_c$. As pointed out in Ref. [27], the Chern-number transfer should always be $\Delta C = 2$ in the case of a critical quadratic band touching. This can also be understood based on the symmetry of the orbitals. At the M point, d_{z^2} and $d_{x^2-y^2}$ states are both eigenstates of the C_4 symmetry operator, but with eigenvalues of $+1$ and -1, respectively. If these labels had been adjacent in the cycle of possible eigenvalues (1, i, -1, $-i$, ...), a Chern transfer $\Delta C = \pm 1$ would have been expected; but because they are not, we get $\Delta C = \pm 2$ [28].

Finally, we note that since the minimum avoided crossings are not in general located on the high-symmetry X-M or Γ-M k path when octahedral rotations are present, the actual band gap is smaller than the one obtained from a band structure plotted along the Γ-X-M-Γ high-symmetry lines. For example, a direct inspection of Fig. 2(a) suggests a gap of 30 meV, compared to the true value of 25 meV obtained from a more careful scan over the full 2D BZ.

III. FIRST-PRINCIPLES CALCULATIONS

In this section, we demonstrate how the tight-binding model discussed above can be realized in more realistic systems. The spin-polarized half-filled e_g states could be realized by a d^4 or d^9 configuration, while non-spin-polarized sublattice could be populated by d^0, d^6, or d^{10} ions. In this work we considered a specific system consisting of a monolayer of LMIO sandwiched into an LAO environment, as shown in Fig. 1(a), although the realization of the tight-binding model is not limited to this specific system. We have chosen LAO as the host environment because it has a large bulk gap of 5.6 eV, so that the states around the Fermi energy (E_F) will be dominated by the orbitals in the LMIO layers.

Our first-principles calculations are done using the projector augmented wave method as implemented in VASP [29]. The exchange-correlation potentials are approximated using the Perdew-Burke-Ernzerhof functionals [30]. For all the structures considered, the in-plane lattice constants are fixed at 3.789 Å, the cubic lattice constant of bulk LAO. For the self-consistent total-energy calculations, the plane-wave energy cutoff is taken to be 500 eV. All our calculations are carried out using the $\sqrt{2} \times \sqrt{2} \times 3$ supercell shown in Fig. 1(a), which also accommodates octahedral rotations about the z axis, and a k-point set corresponding to an $8 \times 8 \times 4$ mesh in the full BZ is used.

To treat Coulomb interactions for open shells, we applied the GGA+U method [31] with double counting considered in the fully localized limit. Since the t_{2g} shells of Ir are almost fully occupied, the GGA+U corrections are only applied to Mn sites. Initially, our calculations are all carried out with $U = 5.0$ eV and $J = 1.0$ eV [32], corresponding to commonly accepted values for Mn^{3+}. Later, we study the effect of varying the U value on the Mn sites, as discussed in the following. In all our calculations, we assume that the magnetic moments of Mn are ferromagnetically coupled. To shift the $4f$ states of La away from E_F, we impose $U_{4f} = 11$ eV and $J_{4f} = 0.68$ eV as used for other calculations on heterostructures [33]. The AHC is obtained by Wannier interpolation using an effective Hamiltonian constructed in a basis of 128 maximally localized Wannier functions [34] corresponding to all Mn-3d, Ir-5d, and O-2p orbitals in the supercell.

Consider first a hypothetical structure without octahedral rotations, specifically one in which the in-plane Mn-O and Ir-O distances are set to be equal, and the out-of-plane Mn-O distance is set to be 2.0 Å. The first-principles band structure is shown in Fig. 3(a). Due to the strong atomic SOC of Ir atoms, their t_{2g} bands are separated into a group of four lower-lying $J = \frac{3}{2}$ bands and two higher $J = \frac{1}{2}$ bands [35]. On the other hand, it is observed that the $3d$ bands of Mn are significantly spin polarized, with an average exchange splitting of about 2 eV even without a local Hubbard U applied. Therefore, the bands around E_F are mostly a mixture of e_g bands of the majority spin character from Mn and the $J = \frac{1}{2}$ bands from Ir. The e_g states of Mn are half-filled, leading to an atomic magnetic moment of about $4\,\mu_B$. The hybridization of the Ir t_{2g} states with the Mn e_g states induces small (about $0.05\,\mu_B$) magnetic moments on the Ir sites.

Introducing octahedral rotations in the LMIO layers leads to significant changes of the band structure by inducing additional hybridizations. Figure 3(b) shows the band structure with a staggered rotation of the MnO_6 and IrO_6 octahedra of 15° about the z axis, while all the other degrees of freedom remain fixed. Now, only two bands, mainly of Mn $d_{x^2-y^2}$ and d_{z^2} character, are left around E_F, although these orbitals hybridize strongly with the Ir 5d orbitals. Recalling the arguments given above in connection with our tight-binding model, such hybridization is crucial for inducing the effective SOC $\lambda^{(2)}$ in Eq. (1), which in turn helps to give a nontrivial gap. We confirm that the gap is indeed nontrivial, with a quantized AHC of $2\,e^2/h$, by direct calculation as shown in Fig. 3(c). The topological band inversion is also evident in the band structure of Fig. 3(b), where the band characters have clearly exchanged between the conduction and valence bands around the M point. We note that the size of the gap is about 26 meV as measured by the width of the quantized AHC plateau, which is smaller than the gap obtained from inspection along the high-symmetry k path in Fig. 3(b); this is again due to the fact that the avoided-crossing points are not located on the high-symmetry lines [cf. Fig. 2(d)].

To be more realistic, we relaxed the structures by allowing the out-of-plane lattice constant and internal coordinates to vary, but keeping the in-plane lattice constants fixed at those of LAO. We find the relaxed octahedral rotation angle in the LMIO layers to be 15.6°, and the relaxed out-of-plane Mn-O distance is about 2.02 Å. By these measures, the ideal structure discussed above is quite reasonable. However, the most drastic change occurs locally in the MnO_6 octahedra, where the local c/a ratio (i.e., the ratio of apical to in-plane Mn-O bond lengths) increases to 1.06, from 1.02 in the ideal structure. This change results from a contraction of the in-plane Mn-O distances.

Figure 3(d) shows the band structure for the fully relaxed structure. Evidently, the $d_{x^2-y^2}$ bands are shifted to higher energies due to the variations of the onsite energies of the $d_{x^2-y^2}$ and d_{z^2} orbitals caused by the local distortions of the MnO_6 octahedra. The resulting $d_{x^2-y^2}$ and d_{z^2} bands no longer overlap anywhere in the BZ, and as a result the gap at E_F is topologically trivial, as verified by our calculations of the AHC

(not shown). Another consequence of the structural relaxations is that the local conduction-band minimum at Γ has shifted downward and now falls about 120 meV below the conduction-band minimum at M. This is caused by a change in the sign of the hopping parameter between $d_{x^2-y^2}$ orbitals located on NN sites, i.e., t_{1a} in Eq. (1). Thus, even if some means could be found to restore the band inversion at M, this reversal in the energy ordering of the conduction-band minima could prevent the maintenance of a global gap, forcing the system metallic.

To overcome these negative effects of the structural relaxations, which disfavor the topological phase, tensile epitaxial strain can be applied to increase the in-plane lattice constants and decrease the out-of-plane one, thus reducing the local octahedral distortions. Figure 3(e) shows the band structure with a 2% tensile epitaxial strain applied to the LAO substrate. In this case, the $d_{x^2-y^2}$ bands are shifted downward in energy relative to the d_{z^2} bands, once again overlapping with them. The gap opened around M shows a typical anticrossing behavior, as emphasized in the inset of Fig. 3(e), and our calculation of the AHC confirms that it is topologically nontrivial. However, the magnitude of the gap is quite small, only about 1 meV. This is a consequence of the fact that the off-diagonal terms in the Hamiltonian of Eq. (1) vanish as one approaches the M point because of the form of $g_1(\mathbf{k})$ and $g_2(\mathbf{k})$. To our satisfaction, we observe that the $d_{x^2-y^2}$ conduction-band minimum at Γ remains above that at the M point, if only barely (by ∼5 meV), so that the gap around M is a true global gap. We conclude that a tensile strain of at least 2% is needed to obtain the QAH state, and speculate that out-of-plane uniaxial pressure could help further.

Interestingly, increasing the strength of the local Hubbard U on the Mn sites also tends to stabilize the topological phase. Figure 3(f) shows the resulting band structure obtained by increasing the Hubbard parameter to $U = 7$ eV on the Mn sites, with the conditions otherwise the same as in Fig. 3(e) (i.e., relaxed with 2% tensile epitaxial strain). Larger U not only shifts the conduction-band minimum at Γ upwards away from E_F, but also enhances the magnitude of the nontrivial topological gap opened around the M point. The magnitude of the global band gap is calculated to be about 4 meV. This is much smaller than the band gap derived from states along the high-symmetry k path, which is about 25 meV, again because the avoided crossings are not located on the high-symmetry lines as explained in Sec. II. Moreover, significant changes occur in the hybridizations between the valence states, caused by the enhanced local atomic U values on the Mn sites. For instance, the d_{z^2} bands are shifted to lower energies [Fig. 3(e) versus Fig. 3(f)], and the first valence band below E_F acquires more $d_{x^2-y^2}$ character with increasing U because of more significant hybridization with the d states of Ir atoms.

IV. CONCLUSIONS

In conclusion, we have demonstrated the possibility of achieving a quantum anomalous Hall phase on a square lattice via an appropriate pattern of intersite spin-orbit couplings between d orbitals, which can be realized in double-perovskite monolayers. We have shown that for a half-filled manifold of e_g orbitals, an effective SOC can be induced by hybridizing with other d orbitals located on the neighboring sites, even though no direct onsite SOC is present. We have found, in particular, that octahedral rotations can induce an effective SOC between e_g orbitals located on NNN sites. We have demonstrated that a simple tight-binding Hamiltonian encoding the most important features of the interactions gives rise quite generically to a quantum anomalous Hall phase. Then, using first-principles calculations, we have also shown that such a model can be realized in La_2MnIrO_6 monolayers. The gap can be as large as 26 meV in the ideal case. However, there are several open issues that need further investigation for this system. First, we have assumed ferromagnetic order, even though there is some tendency of the magnetic moments of the Mn ions to be coupled antiferromagnetically. For instance, we observed that the antiferromagnetic configuration is about 31 meV lower in energy than the ferromagnetic case for the relaxed structure without strain. Nevertheless, for the hypothetical structure, the ferromagnetic state is more stable, about 28 meV lower in energy than the antiferromagnetic state. Hence, the exchange coupling between neighboring Mn moments is quite sensitive to local distortions, which can hopefully be tuned by epitaxial strain. This problem may also be remedied by choosing a substrate with a magnetic order that can enforce the desired ferromagnetic state. Second, there is the issue of the assumed checkerboard compositional order. Even though both Mn and Ir are 3+ ions, which by itself would give no strong tendency toward ordering within the La_2MnIrO_6 monolayer, we argue that such a tendency may come instead from the substantial difference in the ionic radii. Third, it would be useful to understand the role of correlations in more detail. We have found that the e_g states of Mn are quite localized, leading to flat bands, and enhancing the local Hubbard U favors larger band gaps while maintaining the topological nontriviality. We note that our discussion is currently limited to the GGA+U scheme where the onsite electron interactions are treated in a Hartree-Fock manner, while the interplay of electronic correlations and SOC on the square lattices deserves further investigation from beyond-DFT methods.

Finally, as discussed above, the global gap may not remain open after the contraction of the in-plane Mn-O distances with relaxation. We have shown that this problem may be overcome by engineering structures utilizing tensile epitaxial strain of about 2%, making use of the sensitivity of the relevant $d_{x^2-y^2}$ and d_{z^2} bands to local distortions. Further stabilization of the QAH phase might be achieved by varying the choice of the inert perovskite surrounding material, by applying vertical uniaxial pressure in addition to the tensile epitaxial strain, or by chemical doping within the double-perovskite layer or in the surrounding material. Other combinations of transition-metal ions, in which one has a half-filled e_g shell, should also be explored. Lastly, we suspect that the idea of intersite SOC on the square lattices should be applicable to ions with partially filled t_{2g} shells as well. These interesting questions are left for future investigations.

ACKNOWLEDGMENT

This work was supported by NSF Grant No. DMREF-12-33349.

APPENDIX: SYMMETRY ANALYSIS OF THE TWO-BAND MODEL

For the two-band model we considered in the main text, it can be decomposed following

$$H = h_0\sigma_0 + h_1\sigma_x + h_2\sigma_y + h_3\sigma_z, \tag{A1}$$

where σ_0 denotes the unit matrix and σ_i $(i = x,y,z)$ denote the Pauli matrices. We note that h_i $(i = 0,1,2,3)$ can be written as $h_i = h_i' + h_i''$, where h_i' and h_i'' indicate the matrix elements for hopping to the nearest neighbors (NNs) and next-nearest neighbors (NNNs), respectively.

The symmetry operators we considered are $\mathcal{C}_4$, $\mathcal{C}_2$, M_y', and M_d', as shown in Figs. 4 and 5. The $\mathcal{C}_4$ symmetry relates hoppings in directions φ and $\varphi + 90^\circ$ in an obvious way, but does not impose constraints on the form of the hoppings themselves. Moreover, both $\mathcal{C}_2$ operations are symmetries even when octahedral rotations are present, and act at mid-bond positions as shown in Figs. 4 and 5. Examining the transformation of the Hamiltonian matrix elements reveals that $H_{\alpha\beta} = H_{\beta\alpha}^*$. That is, H is Hermitian, so that h_i $(i = 0,1,2,3)$ in Eq. (A1) are real functions of $\mathbf{k}$.

Further constraints on the form of the Hamiltonian can be obtained for the following two situations.

(1) When there are no octahedral rotations (cf. Fig. 4): In this case, both M_y' and M_d' are symmetry operators:

(i) Applying M_y' to the NN hoppings reveals that $h_1' = 0$.

(ii) Applying M_d' to the NNN hoppings reveals that $h_2'' = 0$.

That is, for the off-diagonal term, only h_2' and h_1'' are allowed by symmetry, which correspond to the $\lambda^{(1)}$ term and the t_{2c} term in our Hamiltonian in the main text, respectively.

(2) When there are finite octahedral rotations: In this case, both M_y' and M_d' relate the cases with positive and negative octahedra-rotational angles. For instance,

$$\text{Config}\,(\theta) = M_y'\,\text{Config}\,(-\theta),$$
$$\text{Config}\,(\theta) = M_d'\,\text{Config}\,(-\theta),$$

where Config $(\pm\theta)$ denotes the configuration with positive/negative rotational angle θ:

(i) Applying M_y' to the NN hoppings reveals that $h_1'(-\theta) = -h_1'(\theta)$, and $h_2'(-\theta) = h_2'(\theta)$. That is, h_1' (h_2') is an odd (even) function of rotational angle θ.

(ii) Applying M_d' to the NNN hoppings reveals that $h_1''(-\theta) = h_1''(\theta)$, and $h_2''(-\theta) = -h_2''(\theta)$. That is, h_1'' (h_2'') is an even (odd) function of rotational angle θ.

In this sense, when the octahedral rotations are switched on, h_1' and h_2'' are allowed, which correspond to the t_{1c} term and $\lambda^{(2)}$ term in our Hamiltonian in the main text, respectively.

In short, following the symmetry argument, both $\lambda^{(1)}$ and t_{2c} are even functions of the rotational angle θ, and both $\lambda^{(2)}$ and t_{1c} are odd functions of the rotational angle θ. We note that $\lambda^{(1)}$, $\lambda^{(2)}$, t_{1c}, and t_{2c} can be grouped into $\{\lambda^{(1)}, t_{2c}\}$ and $\{\lambda^{(2)}, t_{1c}\}$, which act separately to induce nontrivial topological properties of the system. As discussed above, $\{\lambda^{(1)}, t_{2c}\}$ are finite without octahedral rotations and can be shown to be even functions of the octahedra-rotation angle θ, while $\{\lambda^{(2)}, t_{1c}\}$ are not allowed by symmetry when $\theta = 0$ and are odd functions of θ. Our tight-binding derivation using the Slater-Koster parameters confirms also this picture, and two important effective spin-orbit coupling parameters $\lambda^{(1)}$ and $\lambda^{(2)}$ are given explicitly in Eqs. (2) and (3) in the main text. We also note that either $\{\lambda^{(1)}, t_{2c}\}$ or $\{\lambda^{(2)}, t_{1c}\}$ can lead to nontrivial topological phases (as shown in Fig. 2 in the main text), with opposite resulting Chern numbers. The final state is determined by the competition between these two groups of parameters, and we observed that the $\{\lambda^{(2)}, t_{1c}\}$ term would be dominant due to $|\lambda^{(2)}| > |\lambda^{(1)}|$. This is confirmed by our first-principles calculations, and detailed discussion is given in the main text.

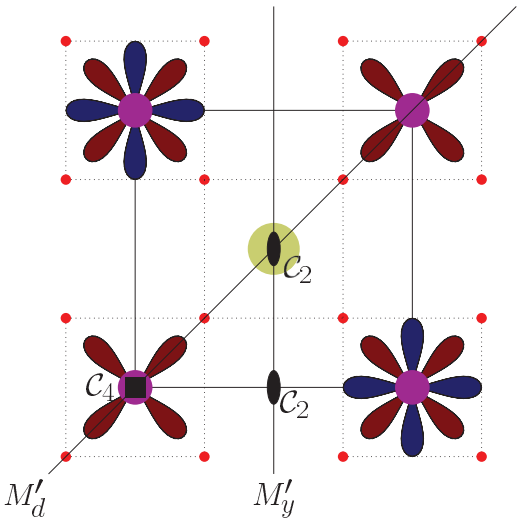

FIG. 4. (Color online) Symmetry operations without octahedral rotations. M' means a combined mirror and time-reversal operation.

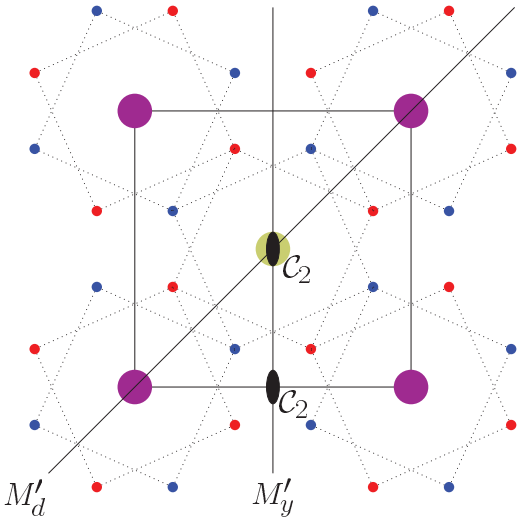

FIG. 5. (Color online) Symmetry operations for La_2MnIrO_6 monolayers with finite octahedral rotations. Red (blue) lattices of oxygen denote octahedral rotations with angle θ $(-\theta)$, which are related to each other by combined mirror and time-reversal operation M'.

[1] F. D. M. Haldane, Phys. Rev. Lett. **61**, 2015 (1988).
[2] C. X. Liu, X.-L. Qi, X. Dai, Z. Fang, and S.-C. Zhang, Phys. Rev. Lett. **101**, 146802 (2008).
[3] R. Yu, W. Zhang, H.-J. Zhang, S.-C. Zhang, X. Dai, and Z. Fang, Science **329**, 61 (2010).
[4] Z. Qiao, S. A. Yang, W. Feng, W.-K. Tse, J. Ding, Y. Yao, J. Wang, and Q. Niu, Phys. Rev. B **82**, 161414 (2010).
[5] H. Zhang, C. Lazo, S. Blügel, S. Heinze, and Y. Mokrousov, Phys. Rev. Lett. **108**, 056802 (2012).
[6] J. Hu, J. Alicea, R. Wu, and M. Franz, Phys. Rev. Lett. **109**, 266801 (2012).
[7] K. F. Garrity and D. Vanderbilt, Phys. Rev. Lett. **110**, 116802 (2013).
[8] Z. F. Wang, Z. Liu, and F. Liu, Phys. Rev. Lett. **110**, 196801 (2013).
[9] C.-Z. Chang, J. Zhang, X. Feng *et al.*, Science **340**, 167 (2013).
[10] D. Xiao, W. Zhu, Y. Ran, N. Nagaosa, and S. Okamoto, Nat. Commun. **2**, 596 (2011).
[11] K. Sun, H. Yao, E. Fradkin, and S. A. Kivelson, Phys. Rev. Lett. **103**, 046811 (2009).
[12] S. Raghu, X.-L. Qi, C. Honerkamp, and S.-C. Zhang, Phys. Rev. Lett. **100**, 156401 (2008).
[13] J. Maciejko, V. Chua, and G. A. Fiete, Phys. Rev. Lett. **112**, 016404 (2014).
[14] C. Wu and S.-C. Zhang, Phys. Rev. Lett. **93**, 036403 (2004).
[15] K.-Y. Yang, W. Zhu, D. Xiao, S. Okamoto, Z. Wang, and Y. Ran, Phys. Rev. B **84**, 201104 (2011).
[16] A. Rüegg and G. A. Fiete, Phys. Rev. B **84**, 201103 (2011).
[17] A. M. Cook and A. Paramekanti, Phys. Rev. Lett. **113**, 077203 (2014).
[18] M. Gibert, P. Zubko, R. Scherwitzl, J. Íñiguez, and J.-M. Triscone, Nat. Mater. **11**, 195 (2012).
[19] X. Chen, S. Dong, and J.-M. Liu, Phys. Rev. B **81**, 064420 (2010).
[20] Y.-X. Wang, F.-X. Li, and Y.-M. Wu, Europhys. Lett. **99**, 47007 (2012).
[21] S. Yang, Z.-C. Gu, K. Sun, and S. Das Sarma, Phys. Rev. B **86**, 241112 (2012).
[22] X. Guo, X. Ren, G. Guo, and J. Peng, Can. J. Phys. **92**, 420 (2014).
[23] H. Zhang, J. Wang, G. Xu, Y. Xu, and S.-C. Zhang, Phys. Rev. Lett. **112**, 096804 (2014).
[24] K. F. Garrity and D. Vanderbilt, Phys. Rev. B **90**, 121103 (2014).
[25] T.-Y. Cai, X. Li, F. Wang, J. Sheng, J. Feng, and C.-D. Gong, arXiv:1310.2471.
[26] G. Logvenov, A. Gozar, and I. Bozovic, Science **326**, 699 (2009).
[27] J. Bellissard, arXiv:cond-mat/9504030.
[28] C. Fang, M. J. Gilbert, X. Dai, and B. A. Bernevig, Phys. Rev. Lett. **108**, 266802 (2012).
[29] http://www.vasp.at
[30] J. P. Perdew, K. Burke, and M. Ernzerhof, Phys. Rev. Lett. **77**, 3865 (1996).
[31] A. I. Liechtenstein, V. I. Anisimov, and J. Zaanen, Phys. Rev. B **52**, R5467(R) (1995).
[32] E. Pavarini and E. Koch, Phys. Rev. Lett. **104**, 086402 (2010).
[33] S. Okamoto, A. J. Millis, and N. A. Spaldin, Phys. Rev. Lett. **97**, 056802 (2006).
[34] A. A. Mostofi, J. R. Yates, Y.-S. Lee, I. Souza, D. Vanderbilt, and N. Marzari, Comput. Phys. Commun. **178**, 685 (2008).
[35] B. J. Kim, H. Jin, S. J. Moon *et al.*, Phys. Rev. Lett. **101**, 076402 (2008).